Comput Mech (2010) 46:703–719
DOI 10.1007/s00466-010-0511-3

ORIGINAL PAPER

Free vibration analysis of thin plates using Hermite reproducing kernel Galerkin meshfree method with sub-domain stabilized conforming integration

Dongdong Wang · Zhenting Lin

Received: 7 February 2010 / Accepted: 8 June 2010 / Published online: 24 June 2010

Abstract A Hermite reproducing kernel (HRK) Galerkin meshfree formulation is presented for free vibration analysis of thin plates. In the HRK approximation the plate deflection is approximated by the deflection as well as slope nodal variables. The nth order reproducing conditions are imposed simultaneously on both the deflectional and rotational degrees of freedom. The resulting meshfree shape function turns out to have a much smaller necessary support size than its standard reproducing kernel counterpart. Obviously this reduction of minimum support size will accelerate the computation of meshfree shape function. To meet the bending exactness in the static sense and to remain the spatial stability the domain integration for stiffness as well as mass matrix is consistently carried out by using the sub-domain stabilized conforming integration (SSCI). Subsequently the proposed formulation is applied to study the free vibration of various benchmark thin plate problems. Numerical results uniformly reveal that the present method produces favorable solutions compared to those given by the high order Gauss integration (GI)-based Galerkin meshfree formulation. Moreover the effect of sub-domain refinement for the domain integration is also investigated.

Keywords Hermite reproducing kernel approximation · Meshfree method · Free vibration · Thin plate · Sub-domain stabilized conforming integration

D. Wang (✉) · Z. Lin
Department of Civil Engineering, Xiamen University, Xiamen 361005, Fujian, China
e-mail: ddwang@xmu.edu.cn

1 Introduction

Free vibration analysis of thin plates in search for the natural frequencies and vibration modes is of great importance and practical interests for the structural dynamic analysis and design. The C^1 continuity requirement for trial and test functions associated with the variational formulation of thin plates in which the shear deformation is neglected often causes severe difficulty for the conventional widely used finite element method since the construction of C^1 conforming finite element approximation is not trivial. While on the other hand in the category of meshfree methods [1–7] which have gained significant research attention during the past twenty years the approximation of field variable can be customized with arbitrary global smoothness in a very straightforward manner. More detailed sate of art review and summary of meshfree methods can be found in [8–12]. Among the versatile meshfree methods developed up to date the moving least-squares (MLS) [1,13] and reproducing kernel (RK) approximations [4,5] are widely used. It turns out that if monomial basis is employed the MLS and RK approaches lead to an identical meshfree approximation. A desirable order of continuity like C^1 in the MLS/RK approximation can be easily achieved under random particle distributions. Consequently meshfree methods provide an ideal way for numerical analysis of thin plate structures.

By taking the advantage of the smooth MLS/RK approximation, Krysl and Belytschko first introduced the element free Galerkin method to analyze thin plate and shell problems [14,15]. Later this method has been applied to the vibration analysis of thin plate and shell problems by Liu and Chen [16] and Liu et al. [17]. Li et al. directly employed the three dimensional reproducing kernel particle method for analysis of large deformation thin shell structures [18]. This approach has been further extended by Qian et al. [19] to study thin

cylinder failure under the combining thermal and mechanical loads. Zhou et al. [20] adopted the reproducing kernel particle method to investigate the free vibration of thin beams and plates. Long and Atluri [21] also proposed a meshless local Petrov Galerkin method for thin plate problems. Rabczuk et al. [22] developed a meshfree thin shell formulation for nonlinear dynamic fracture analysis. In a series of works Liu, Li and their collaborators [23–27] systematically developed a novel reproducing kernel element method for thin plate analysis, where the concept of Hermite-type interpolations in the context of reproducing kernels was proposed. The radial basis function method was applied as well to the vibration analysis of thin plates by Chen et al. [28]. Liu et al. [29] used a Hermite radial point interpolation method for thin plate analysis. More recently the Hermite radial point interpolation method has been implemented by Cui et al. [30] in the context of gradient smoothing method proposed by Chen et al. [31] to model thin plates.

For the aforementioned Galerkin type of meshfree methods it is inevitable to evaluate the stiffness using numerical approaches such as the Gauss quadrature. Due to the rational nature of MLS/RK shape functions, higher order quadrature with demanding CPU cost is often necessary to properly integrate the stiffness. This is more prominent for thin plate problems since the 2nd order derivatives of the test and trial functions are involved in the weak form and thus even much higher order qurdature is required to facilitate the meshfree solution. Therefore computational efficiency has been a major concern related to the Galerkin meshfree method. As a result many efforts have been spent on the development of efficient Galerkin meshfree methods with the necessary property of stability [32–35]. In [32], Beissel and Belytschko proposed a nodal integration meshfree method by adding the residual square of the equilibrium equation to the potential energy functional. Through a gradient smoothing technique Chen et al. [34,35] developed a method of stabilized conforming nodal integration (SCNI) for Galerkin meshfree formulations. This method does not involve any artificial stability parameters and satisfies the linear exactness condition. Later the SCNI method has been systematically developed for shear deformable beams, plates, and shells where the bending exactness was emphasized [36–42]. However subsequently it was observed that the SCNI method designed for the 2nd order differential equations such as elasticity and shear deformable plates and shells does not give satisfactory solutions for thin plate problems where the governing equation is 4th order [43,44].

For thin plate problems, in [43,44] a Hermite reproducing kernel (HRK) approximation and a sub-domain stabilized conforming integration (SSCI) method were developed. In this method the plate rotational and deflectional nodal degrees of freedom are combined together to construct the HRK approximation for the primary field variable of plate deflection. The HRK approximation shows better kernel stability with a smaller minimum normalized support size compared with that of the standard RK approximation. Meanwhile better accuracy was observed in the HRK approximation over the standard RK approximation accordingly. To maintain the stability more representative sub-domains were considered in the integration of stiffness matrix. It was shown that the proposed method performed very well for benchmark static plate problems. In this paper this approach is further introduced into the vibration analysis of thin plates. Both stiffness and consistent mass matrices are consistently constructed by using the SSCI method. Detailed study is performed to verify the effectiveness of the proposed meshfree procedure. Moreover the effect associated with the number of sub-domains used as numerical quadrature is also discussed.

Following this introduction the basic equations for thin plate vibration and the HRK meshfree approximation are presented in Sect. 2. In Sect. 3 the SSCI method is introduced for vibration analysis. The proposed method is demonstrated by benchmark numerical examples in Sect. 4. Section 5 presents a refined study on the solution accuracy of SSCI with increasing number of integration sub-domains. Finally the conclusions are drawn in Sect. 6.

2 Basic equations

2.1 Kinematics of thin plate

Consider a thin plate which occupies a domain $\mathcal{B} = \Omega \times (-t/2, t/2)$, where $\Omega \in \mathbb{R}^2$ denotes the plate mid-plane enclosed by a boundary Γ and t is the plate thickness, respectively. According to the classical Kirchhoff hypothesis for thin plate, all the strain and stress measures can be expressed by the transverse deflection of the middle surface: $w(\boldsymbol{x}), \boldsymbol{x} = \{x, y\} \in \Omega$. The sign conventions of deflection and rotations used in this paper are shown in Fig. 1. Accordingly, the rotation $\boldsymbol{\theta}(\boldsymbol{x})$ and the curvature $\boldsymbol{\kappa}(\boldsymbol{x})$ can be expressed by the primary dependent variable, the deflection $w(\boldsymbol{x})$, as:

$$\boldsymbol{\theta}(\boldsymbol{x}) = \begin{Bmatrix} \theta_x(\boldsymbol{x}) \\ \theta_y(\boldsymbol{x}) \end{Bmatrix} = \begin{Bmatrix} w_{,x}(\boldsymbol{x}) \\ w_{,y}(\boldsymbol{x}) \end{Bmatrix} \tag{1}$$

$$\boldsymbol{\kappa}(\boldsymbol{x}) = \begin{Bmatrix} \kappa_{xx}(\boldsymbol{x}) \\ \kappa_{yy}(\boldsymbol{x}) \\ 2\kappa_{xy}(\boldsymbol{x}) \end{Bmatrix} = \begin{Bmatrix} w_{,xx}(\boldsymbol{x}) \\ w_{,yy}(\boldsymbol{x}) \\ 2w_{,xy}(\boldsymbol{x}) \end{Bmatrix} \tag{2}$$

Based on the isotropic linear constitutive law, the moment vector of stress resultants, $\boldsymbol{m}$, is related to the curvature $\boldsymbol{\kappa}(\boldsymbol{x})$ via:

$$\boldsymbol{m} = \begin{Bmatrix} m_{xx} \\ m_{yy} \\ m_{xy} \end{Bmatrix} = -\boldsymbol{D}\boldsymbol{\kappa} \tag{3}$$

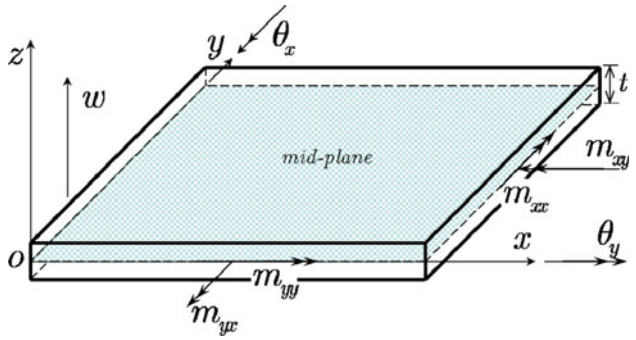

Fig. 1 Sign conventions for thin plate

where $\boldsymbol{D}$ is plate constitutive matrix given as follows:

$$\boldsymbol{D} = \frac{Et^3}{12(1-\upsilon^2)}\begin{bmatrix} 1 & \upsilon & 0 \\ \upsilon & 1 & 0 \\ 0 & 0 & (1-\upsilon)/2 \end{bmatrix} \tag{4}$$

with E and υ being the Young's modulus and Poisson ratio, respectively.

The weak form that governs the dynamics of a thin plate can be stated as follows:

$$\int_\Omega \delta w \rho t \ddot{w} d\Omega + \int_\Omega \delta \boldsymbol{\kappa}^T \boldsymbol{D} \boldsymbol{\kappa}^T d\Omega - \delta W^{\text{ext}} = 0 \tag{5}$$

where ρ is the material density, the superposed double dots over w denote the twice time differentiation. δW^{ext} is associated with the applied external loads and in the free vibration analysis one has $\delta W^{\text{ext}} = 0$.

2.2 HRK approximation

The HRK [44] approximation is a generalization of the standard RK [4–7] approximation via including the first order derivatives through the reproducing or consistency conditions into the approximation of the primary field variable, say, the plate deflection $w(\boldsymbol{x})$ in this work. In HRK approximation, the mid-plane domain Ω is discretized by a set of meshfree particles $\boldsymbol{x}_I$, $I = 1, 2, \ldots, NP$, the nodal vector $\boldsymbol{d}_I$ associated with particle I carries three unknown variables, i.e., $\boldsymbol{d}_I = \{w_I, \theta_{xI}, \theta_{yI}\}^T$, and the HRK approximation of the deflection $w(\boldsymbol{x})$, denoted by $w^h(\boldsymbol{x})$, can be expressed as:

$$\begin{aligned} w^h(\boldsymbol{x}) &= \sum_{I=1}^{NP}\left[\Psi_I^w(\boldsymbol{x})w_I + \Psi_I^{\theta x}(\boldsymbol{x})\theta_{xI} + \Psi_I^{\theta y}(\boldsymbol{x})\theta_{yI}\right] \\ &= \sum_{I=1}^{NP} \boldsymbol{\Psi}_I(\boldsymbol{x})\boldsymbol{d}_I \end{aligned} \tag{6}$$

where $\boldsymbol{\Psi}_I(\boldsymbol{x}) = \{\Psi_I^w(\boldsymbol{x}), \Psi_I^{\theta x}(\boldsymbol{x}), \Psi_I^{\theta y}(\boldsymbol{x})\}$, $\Psi_I^w(\boldsymbol{x})$, $\Psi_I^{\theta x}(\boldsymbol{x})$ and $\Psi_I^{\theta y}(\boldsymbol{x})$ are the deflectional and rotational shape functions of node I, which take the following form:

$$\Psi_I^w(\boldsymbol{x}) = \boldsymbol{p}^T(\boldsymbol{x_I} - \boldsymbol{x})\boldsymbol{b}(\boldsymbol{x})\phi_a(\boldsymbol{x_I} - \boldsymbol{x}) \tag{7}$$

$$\Psi_I^{\theta x}(\boldsymbol{x}) = \boldsymbol{p}_x^T(\boldsymbol{x_I} - \boldsymbol{x})\boldsymbol{b}(\boldsymbol{x})\phi_a(\boldsymbol{x_I} - \boldsymbol{x}) \tag{8}$$

$$\Psi_I^{\theta y}(\boldsymbol{x}) = \boldsymbol{p}_y^T(\boldsymbol{x_I} - \boldsymbol{x})\boldsymbol{b}(\boldsymbol{x})\phi_a(\boldsymbol{x_I} - \boldsymbol{x}) \tag{9}$$

where $\boldsymbol{b}(\boldsymbol{x})$ is the unknown position dependent coefficient vector to be solved. $\phi_a(\boldsymbol{x_I} - \boldsymbol{x})$ is the kernel function centering at node I which has a compact support measured by 'a'. In this work the cubic B-spline kernel function is employed [7]. The nth order monomial basis vectors $\boldsymbol{p}, \boldsymbol{p}_x$, and $\boldsymbol{p}_y$ are defined as:

$$\boldsymbol{p}(\boldsymbol{x}) = \left\{1, x, y, x^2, xy, y^2, \ldots, x^n, \ldots, y^n\right\}^T \tag{10}$$

$$\boldsymbol{p}_x(\boldsymbol{x}) = \frac{\partial \boldsymbol{p}(\boldsymbol{x})}{\partial x} = \left\{0, 1, 0, 2x, y, 0, \ldots, nx^{n-1}, \ldots, 0\right\}^T \tag{11}$$

$$\boldsymbol{p}_y(\boldsymbol{x}) = \frac{\partial \boldsymbol{p}(\boldsymbol{x})}{\partial y} = \left\{0, 0, 1, 0, x, 2y, \ldots, 0, \ldots, ny^{n-1}\right\}^T \tag{12}$$

The coefficient vector $\boldsymbol{b}(\boldsymbol{x})$ is solved by imposing the following nth order reproducing conditions:

$$\begin{aligned} \sum_{I=1}^{NP}\Big[&\Psi_I^w(\boldsymbol{x})\boldsymbol{p}(\boldsymbol{x_I} - \boldsymbol{x}) + \Psi_I^{\theta x}(\boldsymbol{x})\boldsymbol{p}_x(\boldsymbol{x_I} - \boldsymbol{x}) \\ &+\Psi_I^{\theta y}(\boldsymbol{x})\boldsymbol{p}_y(\boldsymbol{x_I} - \boldsymbol{x})\Big] = \boldsymbol{p}(\boldsymbol{0}) \end{aligned} \tag{13}$$

Substituting Eqns. (7)–(9) into Eq. (13) yields:

$$\boldsymbol{\mathcal{M}}(\boldsymbol{x})\boldsymbol{b}(\boldsymbol{x}) = \boldsymbol{p}(\boldsymbol{0}) \tag{14}$$

where $\boldsymbol{\mathcal{M}}(\boldsymbol{x})$ is the HRK moment matrix given by:

$$\begin{aligned} \boldsymbol{\mathcal{M}}(\boldsymbol{x}) &= \sum_{I=1}^{NP}\begin{bmatrix}\boldsymbol{p}(\boldsymbol{x_I} - \boldsymbol{x})\boldsymbol{p}^T(\boldsymbol{x_I} - \boldsymbol{x}) + \boldsymbol{p}_x(\boldsymbol{x_I} - \boldsymbol{x})\boldsymbol{p}_x^T(\boldsymbol{x_I} - \boldsymbol{x}) \\ +\boldsymbol{p}_y(\boldsymbol{x_I} - \boldsymbol{x})\boldsymbol{p}_y^T(\boldsymbol{x_I} - \boldsymbol{x})\end{bmatrix} \\ &\quad \times\phi_a(\boldsymbol{x_I} - \boldsymbol{x}) \\ &= \boldsymbol{\mathcal{M}}^0(\boldsymbol{x}) + \boldsymbol{\mathcal{M}}^1(\boldsymbol{x}) \end{aligned} \tag{15}$$

with $\boldsymbol{\mathcal{M}}^0$ and $\boldsymbol{\mathcal{M}}^1$ being defined as:

$$\boldsymbol{\mathcal{M}}^0(\boldsymbol{x}) = \sum_{I=1}^{NP}\boldsymbol{p}(\boldsymbol{x_I} - \boldsymbol{x})\boldsymbol{p}^T(\boldsymbol{x_I} - \boldsymbol{x})\phi_a(\boldsymbol{x_I} - \boldsymbol{x}) \tag{16}$$

$$\begin{aligned} \boldsymbol{\mathcal{M}}^1(\boldsymbol{x}) = \sum_{I=1}^{NP}\Big[&\boldsymbol{p}_x(\boldsymbol{x_I} - \boldsymbol{x})\boldsymbol{p}_x^T(\boldsymbol{x_I} - \boldsymbol{x}) \\ &+\boldsymbol{p}_y(\boldsymbol{x_I} - \boldsymbol{x})\boldsymbol{p}_y^T(\boldsymbol{x_I} - \boldsymbol{x})\Big]\phi_a(\boldsymbol{x_I} - \boldsymbol{x}) \end{aligned} \tag{17}$$

Therefore from Eq. (14) one has $\boldsymbol{b}(\boldsymbol{x}) = \boldsymbol{\mathcal{M}}^{-1}(\boldsymbol{x})\boldsymbol{p}(\boldsymbol{0})$ and the HRK shape functions finally become:

$$\Psi_I^w(\boldsymbol{x}) = \boldsymbol{p}^T(0)\boldsymbol{\mathcal{M}}^{-1}(\boldsymbol{x})\boldsymbol{p}(\boldsymbol{x_I} - \boldsymbol{x})\phi_a(\boldsymbol{x_I} - \boldsymbol{x}) \tag{18}$$

$$\Psi_I^{\theta x}(\boldsymbol{x}) = \boldsymbol{p}^T(0)\boldsymbol{\mathcal{M}}^{-1}(x)\boldsymbol{p}_x(\boldsymbol{x_I} - \boldsymbol{x})\phi_a(\boldsymbol{x_I} - \boldsymbol{x}) \tag{19}$$

$$\Psi_I^{\theta y}(\boldsymbol{x}) = \boldsymbol{p}^T(0)\boldsymbol{\mathcal{M}}^{-1}(\boldsymbol{x})\boldsymbol{p}_y(\boldsymbol{x_I} - \boldsymbol{x})\phi_a(\boldsymbol{x_I} - \boldsymbol{x}) \tag{20}$$

From Eqs. (15) to (17), it is clear that $\mathcal{M}^0(\boldsymbol{x})$ is exactly the moment matrix of the standard RK approximation [4–7], and $\mathcal{M}^1(\boldsymbol{x})$ is an additional term associated with the HRK approximation. It turns out this additional terms leads to better kernel stability for the HRK approximation. In the standard RK approximation it is known that to ensure the invertibility of the moment matrix $\mathcal{M}$, any position $\boldsymbol{x}$ must be covered by at least m independent kernel functions and m is the dimension of basic vector $\boldsymbol{p}$. Thus for a quadratic basis function the normalized support size a is at least to be 2. However it can be shown that for the HRK approximation this requirement is significantly relaxed. This is illustrated next by a typical example.

Consider a 2D problem domain discretized by a set of uniformly spaced particles $\{\boldsymbol{x}_I\}_{I=1}^{NP}$ with nodal distance h, thus the normalized support size a_n can be defined as $a_n = a/h$. As shown in Fig. 2, let $\boldsymbol{x} = \boldsymbol{x}_1 = \{0, 0\}^T$ be a corner node and the normalized support size be $a_n \in (1, 2)$, then the corresponding moment matrices of the standard RK and HRK approximation with a quadratic basis can be expressed as follows:

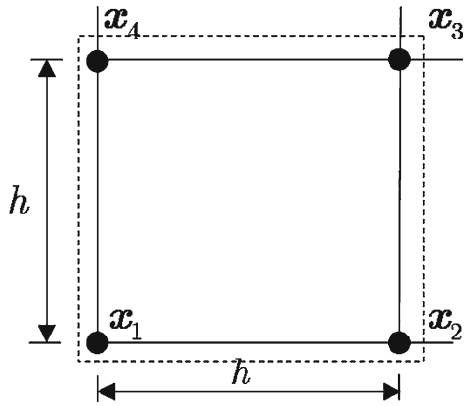

Fig. 2 Nodal support domain for $\boldsymbol{x} = \boldsymbol{x}_1$ with $a_n \in (1, 2)$

$$\mathcal{M}(\boldsymbol{x}_1) \sim \begin{bmatrix} 1 & 0 & 0 & 0 & 0 & 0 \\ 0 & 1 & 0 & 0 & 0 & 0 \\ 0 & 0 & 1 & 0 & 0 & 0 \\ 0 & 0 & 0 & 1 & 0 & 0 \\ 0 & 0 & 0 & 0 & 1 & 0 \\ 0 & 0 & 0 & 0 & 0 & 1 \end{bmatrix} \tag{23}$$

$$\mathcal{M}^0(\boldsymbol{x}_1) = \sum_{I=1}^{4} \mathcal{M}_I^0(\boldsymbol{x}_1) = \begin{bmatrix} \phi^s_{1234} & \phi^s_{23}h & \phi^s_{34}h & \phi^s_{23}h^2 & \phi_3h^2 & \phi^s_{34}h^2 \\ & \phi^s_{23}h^2 & \phi_3h^2 & \phi^s_{23}h^3 & \phi_3h^3 & \phi_3h^3 \\ & & \phi^s_{34}h^2 & \phi_3h^3 & \phi_3h^3 & \phi^s_{34}h^3 \\ & & & \phi^s_{23}h^4 & \phi_3h^4 & \phi_3h^4 \\ & & sym. & & \phi_3h^4 & \phi_3h^4 \\ & & & & & \phi^s_{34}h^4 \end{bmatrix} \tag{21}$$

$$\mathcal{M}(\boldsymbol{x}_1) = \sum_{I=1}^{4} [\mathcal{M}_I^0(\boldsymbol{x}_1) + \mathcal{M}_I^1(\boldsymbol{x}_1)] = \begin{bmatrix} \phi^s_{1234} & \phi^s_{23}h & \phi^s_{34}h & h^2\phi^s_{23} & h^2\phi_3 & h^2\phi^s_{34} \\ & \phi^s_{23}h^2 + \phi^s_{1234} & \phi_3h^2 & (h^3+2h)\phi^s_{23} & (h^3+h)\phi_3 + h\phi_4 & h^3\phi_3 \\ & & \phi^s_{34}h^2 + \phi^s_{1234} & h^3\phi_3 & (h^3+h)\phi_3 + h\phi_2 & (h^3+2h)\phi^s_{34} \\ & & & (h^4+4h^2)\phi^s_{23} & (h^4+2h^2)\phi_3 & h^4\phi_3 \\ & & sym. & & (h^4+2h^2)\phi_3 + h^2\phi^s_{24} & h^4\phi_3 + 2h^2\phi_3 \\ & & & & & (h^4+4h^2)\phi^s_{34} \end{bmatrix} \tag{22}$$

where for brevity ϕ_I denotes the value of the kernel function of Ith node evaluated at the location $\boldsymbol{x}_1$, $\phi^s_{IJ} \triangleq \phi_I + \phi_J$, and $\phi^s_{1234} \triangleq \phi_1 + \phi_2 + \phi_3 + \phi_4$, respectively. Obviously, $\mathcal{M}^0(\boldsymbol{x}_1)$ defined by Eq. (21) is singular by virtue of the fact that the 2nd and 4th rows are linearly dependent. On the other hand it can be shown that the HRK moment matrix $\mathcal{M}(\boldsymbol{x}_1)$ shown in Eq. (22) can be reduced to the following standard simplest form through the elementary matrix row and column transform operations:

Therefore $\mathcal{M}(\boldsymbol{x}_1)$ is non-singular and the HRK shoe functions are well defined for $a_n \in (1, 2)$. This shows that for the quadratic basis the minimum normalized support size of the HRK approximation is 1 while it is 2 for the conventional RK approximation. It demonstrates that the HRK approximation has the property of better kernel stability. Fig. 3 lists the quadratic HRK shape functions of Eqs. (18)–(20) with $a_n = 1$. The exact reproducing properties of quadratic basis functions are also shown in Fig. 4.

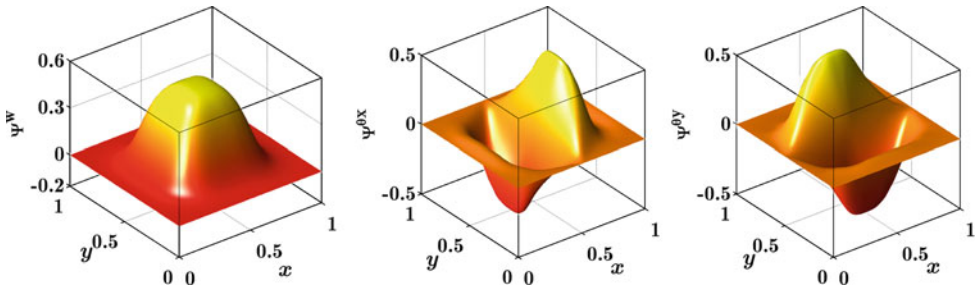

Fig. 3 HRK shape functions with $a_n = 1.0$

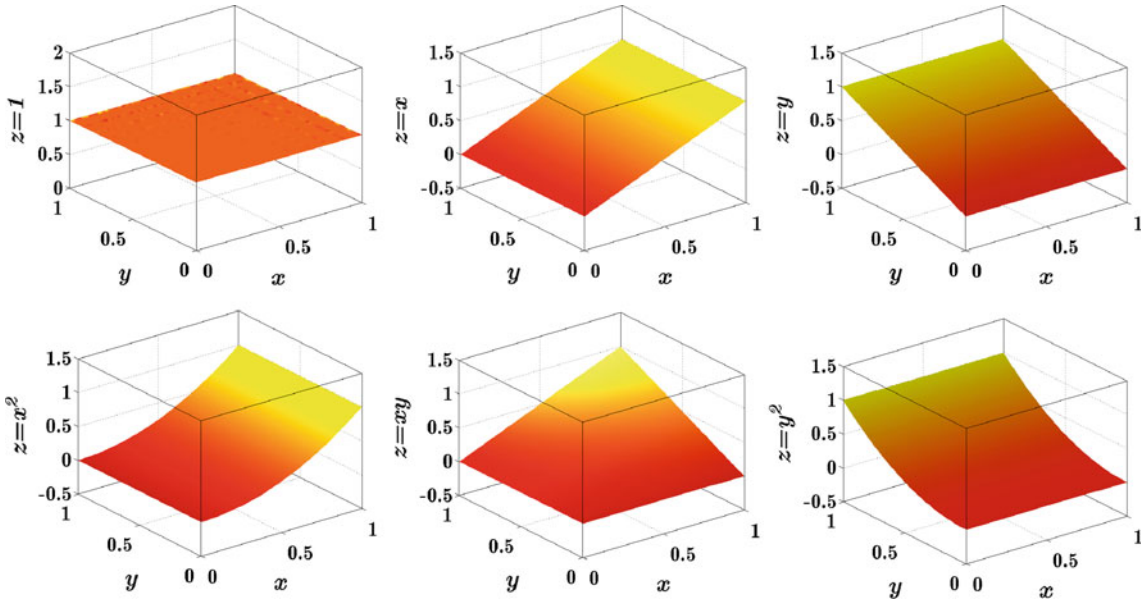

Fig. 4 Reproducing properties of HRK shape functions with $a_n = 1.0$

3 SSCI thin plate formulation

To maintain the spatial stability the SSCI thin plate formulation is fulfilled by the sub-domain integration methodology where the nodal representative domain is further divided into several sub-domains for domain integration and the curvature smoothing is performed in each sub-domain. In this case the integration constraint for bending exactness [43,44] is still exactly satisfied.

3.1 Sub-domain curvature smoothing

As shown in Fig. 5, Ω_L is the nodal representative domain for the particle $\boldsymbol{x}_L$, which is enclosed by the boundary Γ_L. In SSCI Ω_L is sub-divided into LS non-overlapping and conforming sub-domains, i.e., $\bigcup_{L_m=1}^{LS} \Omega_{L_m} = \Omega_L$. The voronoi diagram can be used to produce the nodal representative domain Ω_L as indicated in Fig. 5. Thereafter the sub-domain can be further obtained by subdividing the nodal representative domain through connecting the node and the edge middle points of voronoi diagram. It is noted the only requirement for the sub-domains is to construct conforming cells for domain integration and thus other choices for sub-domains are also possible. The smoothed curvature $\tilde{\boldsymbol{\kappa}}$ in Ω_{L_m} is defined as:

$$\begin{aligned}\tilde{\kappa}_{ij}(\boldsymbol{x}_{L_m}) &= \frac{1}{A_{L_m}} \int_{\Omega_{L_m}} \kappa_{ij}(\boldsymbol{x}) d\Omega \\ &= \frac{1}{2A_{L_m}} \int_{\Omega_{L_m}} (w_{,ij} + w_{,ji}) d\Omega, \\ \{i, j\} &= \{1, 2\} = \{x, y\}\end{aligned} \tag{24}$$

where A_{L_m} denotes the area of Ω_{L_m}. To meet the integration constraint for bending exactness, by using divergence theorem Eq. (24) becomes:

$$\tilde{\kappa}_{ij}(\boldsymbol{x}_{L_m}) = \frac{1}{2A_{L_m}} \int_{\Gamma_{L_m}} (w_{,i} n_j + w_{,j} n_i) d\Gamma \tag{25}$$

with Γ_{L_m} being the boundary of the sub-domain Ω_{L_m} and $\boldsymbol{n} = \{n_i\}$ being the outward normal of Γ_{L_m}.

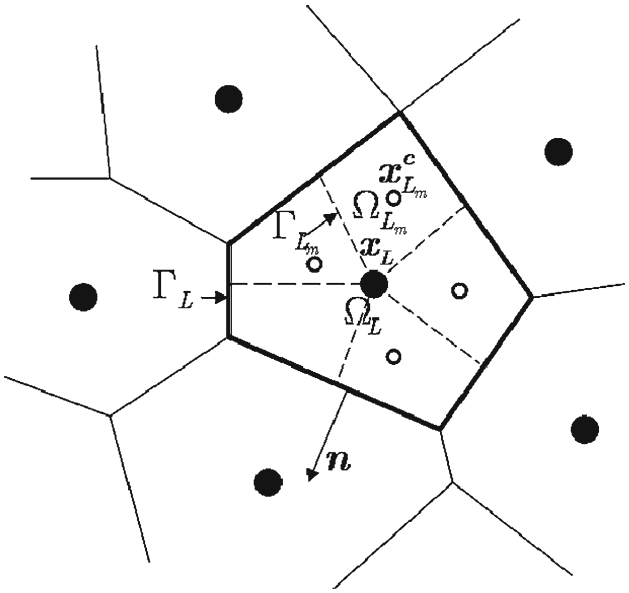

Fig. 5 Nodal representative sub-domains for curvature smoothing and integration

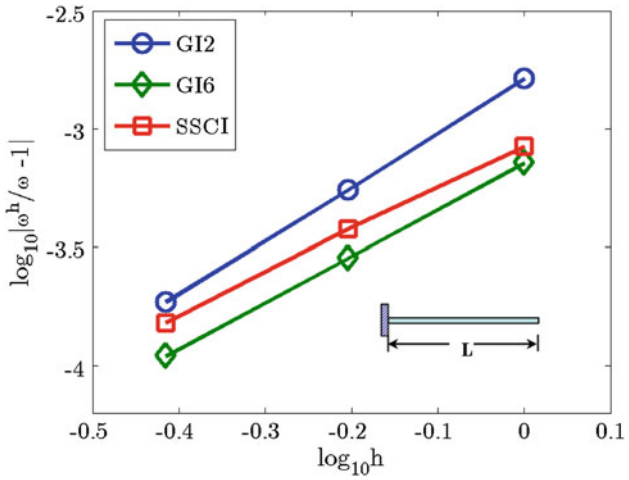

Fig. 6 Comparison of the fundamental frequency for clamped-free beam

Substituting the HRK approximation of Eq. (6) into Eq. (25) gives:

$$\tilde{\kappa}^h_{ij}(\boldsymbol{x}_{L_m}) = \sum_{I=1}^{NP} \frac{1}{2A_{L_m}} \left[\tilde{\nabla}_j \boldsymbol{\Psi}_{I,i}(\boldsymbol{x}_{L_m}) \boldsymbol{d}_I + \tilde{\nabla}_i \boldsymbol{\Psi}_{I,j}(\boldsymbol{x}_{L_m}) \boldsymbol{d}_I \right] \tag{26}$$

with

$$\tilde{\nabla}_j \boldsymbol{\Psi}_{I,i}(\boldsymbol{x}_{L_m}) = \frac{1}{A_{L_m}} \int_{\Gamma_{Lm}} \left[\Psi^w_{I,i}, \Psi^{\theta x}_{I,i}, \Psi^{\theta y}_{I,i} \right] n_j d\Gamma \tag{27}$$

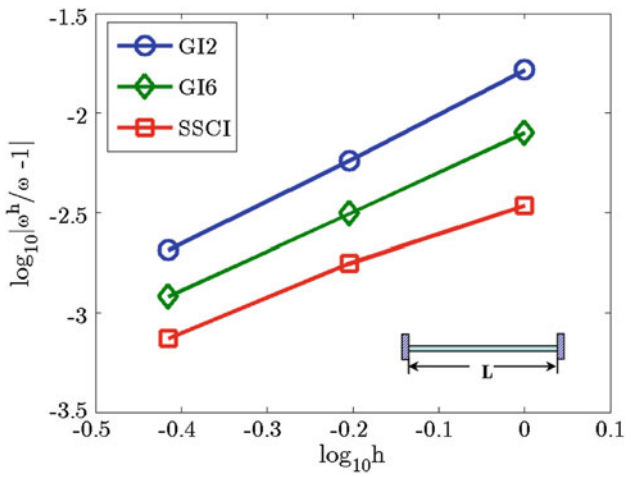

Fig. 7 Comparison of the fundamental frequency for clamped-clamped beam

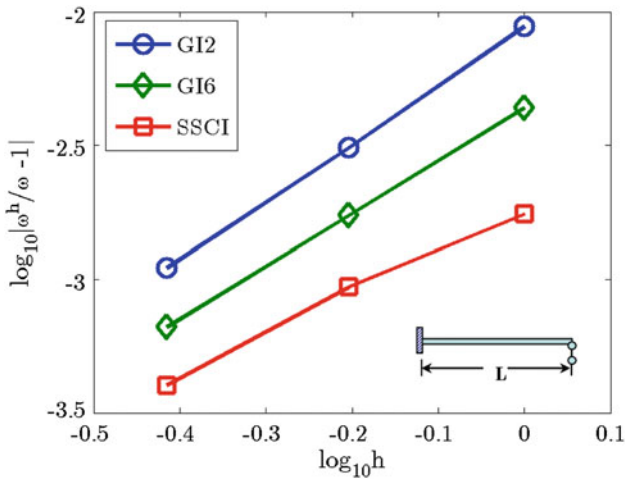

Fig. 8 Comparison of the fundamental frequency for clamped-simply supported beam

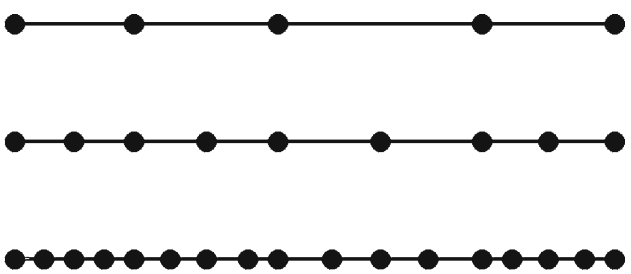

Fig. 9 Irregular meshfree dicretizations for beam problems

In matrix form Eq. (26) can be rearranged as:

$$\tilde{\boldsymbol{\kappa}}^h(\boldsymbol{x}_{L_m}) = \sum_{I=1}^{NP} \tilde{\boldsymbol{B}}_I(\boldsymbol{x}_{L_m}) \boldsymbol{d}_I \tag{28}$$

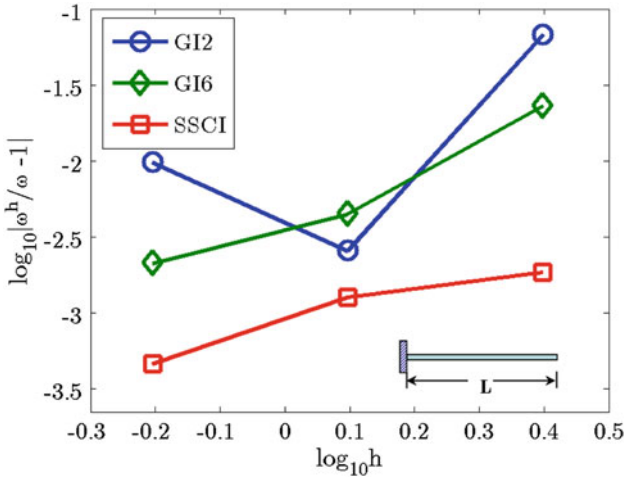

Fig. 10 Comparison of the fundamental frequency for clamped-free beam using irregular meshfree dicretizations

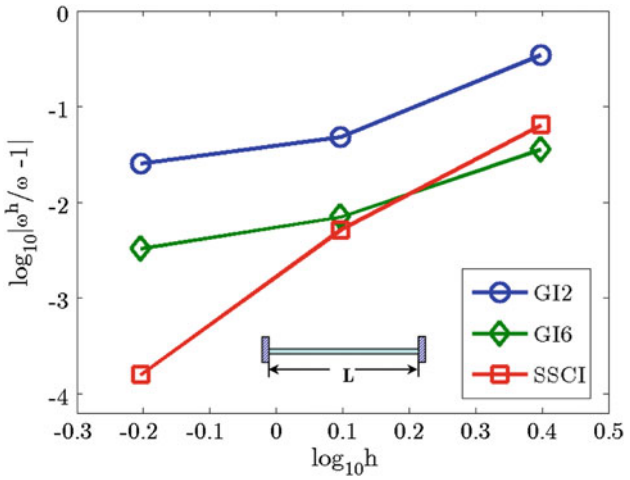

Fig. 11 Comparison of the fundamental frequency for clamped-clamped beam using irregular meshfree dicretizations

where $\tilde{\boldsymbol{B}}_I(\boldsymbol{x}_{L_m})$ is the smoothed gradient matrix given by:

$$\tilde{\boldsymbol{B}}_I(\boldsymbol{x}_{L_m}) = \begin{bmatrix} \tilde{\nabla}_x \Psi^w_{I,x}(\boldsymbol{x}_{L_m}) & \tilde{\nabla}_x \Psi^{\theta x}_{I,x}(\boldsymbol{x}_{L_m}) & \tilde{\nabla}_x \Psi^{\theta y}_{I,x}(\boldsymbol{x}_{L_m}) \\ \tilde{\nabla}_x \Psi^w_{I,y}(\boldsymbol{x}_{L_m}) & \tilde{\nabla}_x \Psi^{\theta x}_{I,y}(\boldsymbol{x}_{L_m}) & \tilde{\nabla}_x \Psi^{\theta y}_{I,y}(\boldsymbol{x}_{L_m}) \\ 2\tilde{\nabla}_y \Psi^w_{I,x}(\boldsymbol{x}_{L_m}) & 2\tilde{\nabla}_y \Psi^{\theta x}_{I,x}(\boldsymbol{x}_{L_m}) & 2\tilde{\nabla}_y \Psi^{\theta y}_{I,x}(\boldsymbol{x}_{L_m}) \end{bmatrix} \tag{29}$$

3.2 Discrete equations

The aforementioned method of SSCI is developed for stiffness matrix integration in order to meet the bending exactness condition and stability requirement. In this study the integration of mass matrix is also carried out by sampling the centroid values of material density over the sub-domains and then multiplying the corresponding sub-domain areas. This provides a consistent and efficient computer implementation

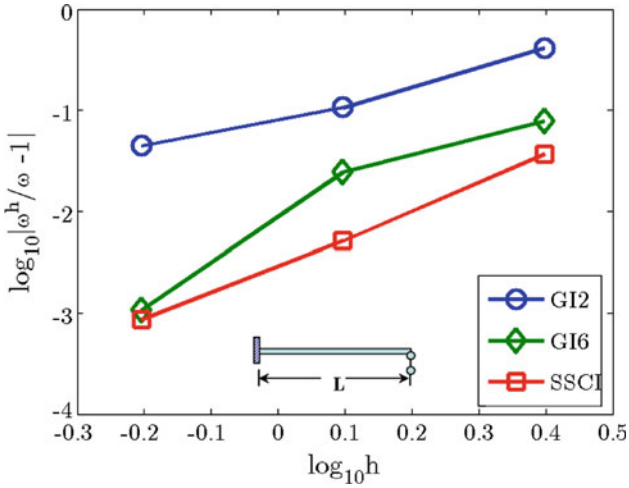

Fig. 12 Comparison of the fundamental frequency for clamped-simply supported beam using irregular meshfree dicretizations

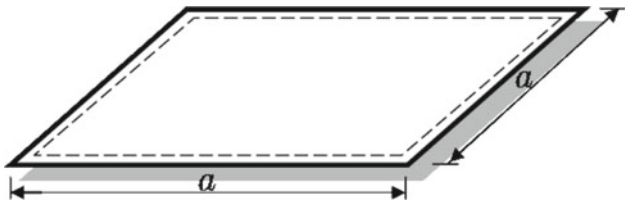

Fig. 13 A simply supported square thin plate

Table 1 List of λs for simply supported square plate

Mode	Analytical [46]	GI2	GI6	SSCI
1	4.443	4.438	4.446	4.442
2	7.025	7.020	7.037	7.025
3	7.025	7.020	7.037	7.025
4	8.886	8.863	8.908	8.877
5	9.935	9.941	9.972	9.946
6	9.935	9.942	9.972	9.946
7	11.327	11.297	11.376	11.316
8	11.327	11.297	11.376	11.317

of the proposed SSCI formulation for vibration problems. By invoking the proposed numerical quadrature rule, the weak form of Eq. (5) for free vibration analysis becomes:

$$\sum_{L=1}^{NP}\sum_{L_m=1}^{LS}\left[\delta w^{hT}(\boldsymbol{x}^c_{L_m})\rho t\, w^h(\boldsymbol{x}^c_{L_m})\right]A_{L_m} + \sum_{L=1}^{NP}\sum_{L_m=1}^{LS}\left[\delta\tilde{\boldsymbol{\kappa}}^{hT}(\boldsymbol{x}_{L_m})\boldsymbol{D}\tilde{\boldsymbol{\kappa}}^h(\boldsymbol{x}_{L_m})\right]A_{L_m} = \boldsymbol{0} \tag{30}$$

where the virtual work related to the applied forces are absent since here only the free vibration is considered, $\boldsymbol{x}^c_{L_m}$ is the centroid of the sub-domain Ω_{L_m} as shown in Fig. 5.

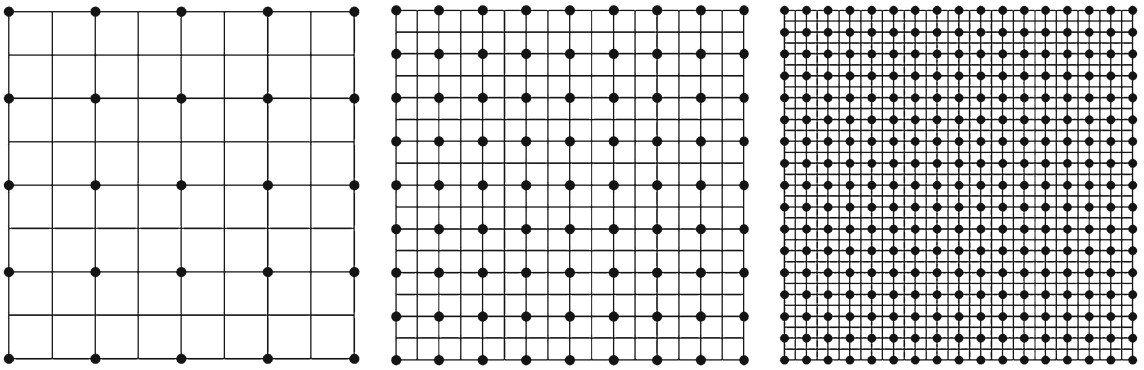

Fig. 14 Meshfree discretizations for square plate

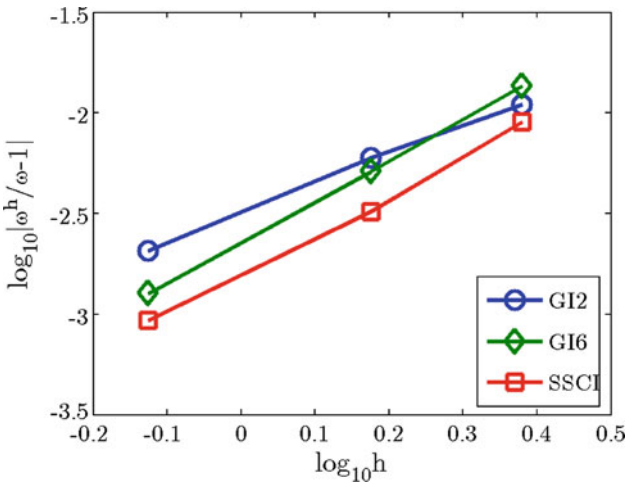

Fig. 15 Comparison of the fundamental frequency for simply supported square plate

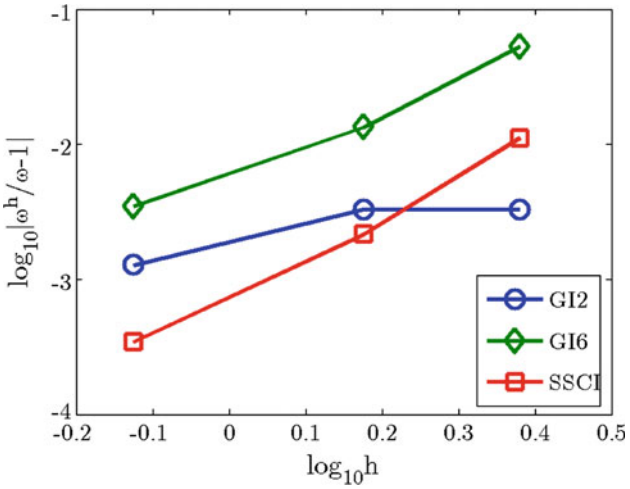

Fig. 16 Comparison of the second frequency for simply supported square plate

Consequently the matrix equation corresponding to Eq. (30) is:

$$\boldsymbol{M}\ddot{\boldsymbol{d}} + \boldsymbol{K}\boldsymbol{d} = \boldsymbol{0} \tag{31}$$

where $\boldsymbol{M}$ and $\boldsymbol{d}$ are the mass and stiffness matrices, respectively:

$$\boldsymbol{M} = \mathop{\mathcal{A}}_{I,J=1}^{NP} \boldsymbol{M}_{IJ}; \quad \boldsymbol{K} = \mathop{\mathcal{A}}_{I,J=1}^{NP} \boldsymbol{K}_{IJ} \tag{32}$$

with $\mathcal{A}$ denoting an assembly operation and sub-matrices of $\boldsymbol{M}_{IJ}$ and $\boldsymbol{K}_{IJ}$ are given by:

$$\boldsymbol{M}_{IJ} = \sum_{L=1}^{NP} \sum_{L_m=1}^{LS} \left[\boldsymbol{\Psi}_I^T(\boldsymbol{x}_{L_m}^c) \rho t \boldsymbol{\Psi}_J(\boldsymbol{x}_{L_m}^c) \right] A_{L_m} \tag{33}$$

$$\boldsymbol{K}_{IJ} = \sum_{L=1}^{NP} \sum_{L_m=1}^{LS} \left[\tilde{\boldsymbol{B}}_I^T(\boldsymbol{x}_{L_m}) \boldsymbol{D} \tilde{\boldsymbol{B}}_J(\boldsymbol{x}_{L_m}) \right] A_{L_m} \tag{34}$$

Fig. 17 Mode shapes for simply supported square plate

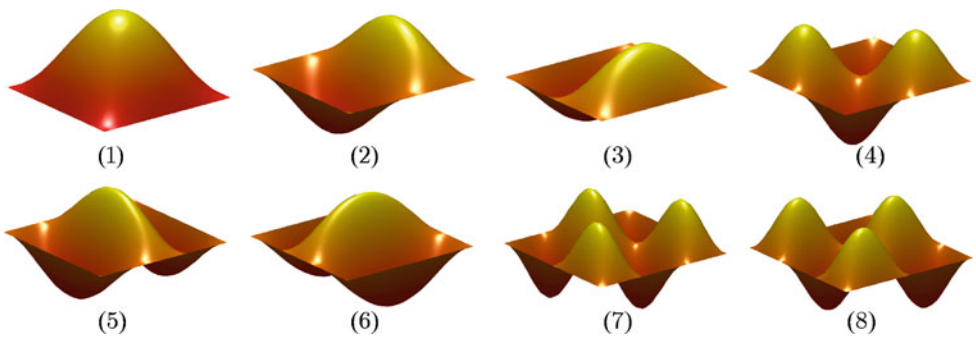

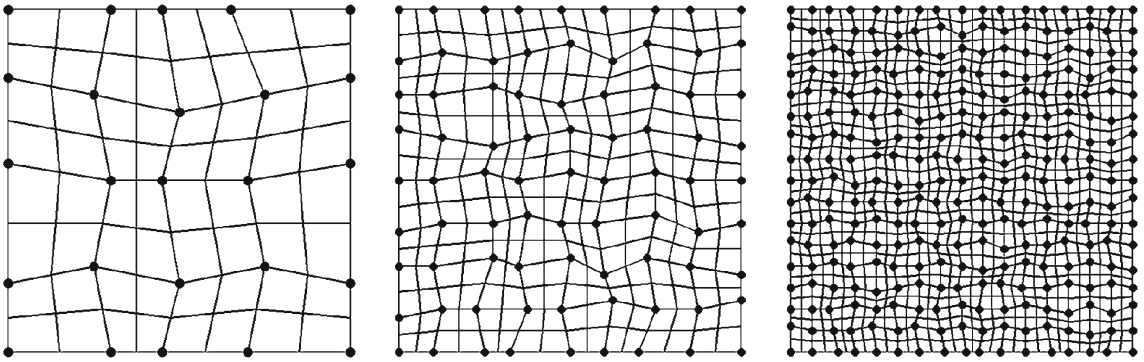

Fig. 18 Irregular discretizations for simply supported square plate

Thus the generalized eigenvalue problem corresponding to Eq. (31) is:

$$(\boldsymbol{K} - \omega^2 \boldsymbol{M})\boldsymbol{\Phi} = \boldsymbol{0} \tag{35}$$

where ω is the natural frequency and $\boldsymbol{\Phi}$ is the associated vibration mode. The boundary conditions during the vibration analysis are efficiently enforced by using the mixed transformation method developed by Chen and Wang [45]. This approach relates the generalized coordinates of deflection and rotations to their corresponding physical coordinates [44] for the boundary constrained particles only.

4 Numerical examples

In this section, several typical thin plate as well as thin beam examples are presented to study the performance of the present method. The thin beam problem is considered here since it is a one dimensional degeneration of thin plate and thus is very helpful to comprehensively illustrate the proposed method. For comparison the Gauss integration (GI)-based HRK formulations are also included in the following examples, where the notation "GIm" denotes the mth order Gauss integration in each dimension. Unless specified in the following examples SSCI implies the integration using 2 subdomains in each dimension.

4.1 Thin beam

Consider a thin beam with length $L = 10$, cross-section width $b = 0.05$, height $t = 0.02$, density $\rho = 2500$, Young's modulus is $E = 2 \times 10^9$. In the analysis a uniform particle distribution is employed in the HRK approximation with a quadratic basis vector. The cubic B-spline function is used as the kernel function with the normalized supported size being 1.3. The convergence comparison of the fundamental frequency using uniform meshfree discretizations is shown in Figs. 6, 7 and 8, where various boundary conditions such as clamped-free, clamped-clamped, and clamped-simply supported, are analyzed. As just stated GI2 and GI6 denote the Gauss integration with 2-point and 6-point quadrature rules in each nodal representative domain and SSCI represents the proposed method with 2 sub-domains. The results clearly show that SSCI gives the most favorable solutions compared to those obtained by GI2 and GI6. Moreover the robustness of the present method is further demonstrated by using the irregular discretizations as shown in Fig. 9 and the

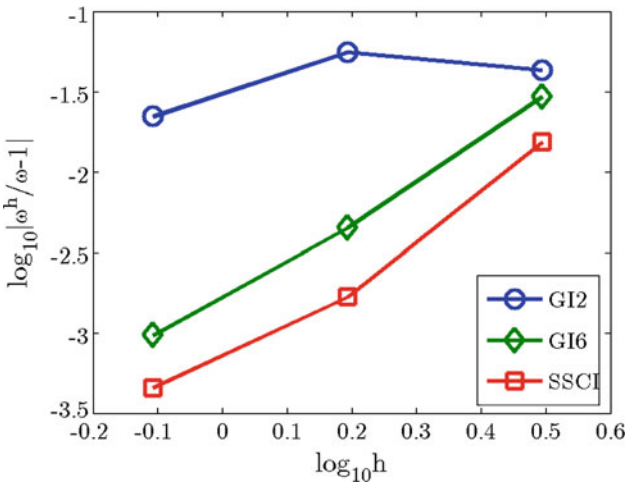

Fig. 19 Comparison of the second frequency for simply supported square plate using irregular discretizations

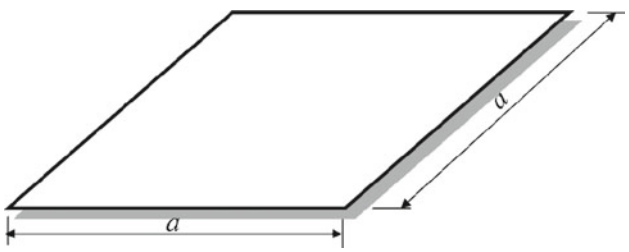

Fig. 20 A clamped square thin plate

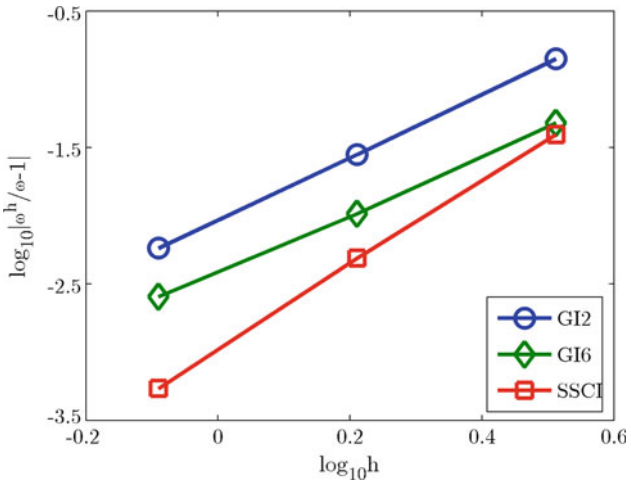

Fig. 21 Comparison of the fundamental frequency for clamped square plate

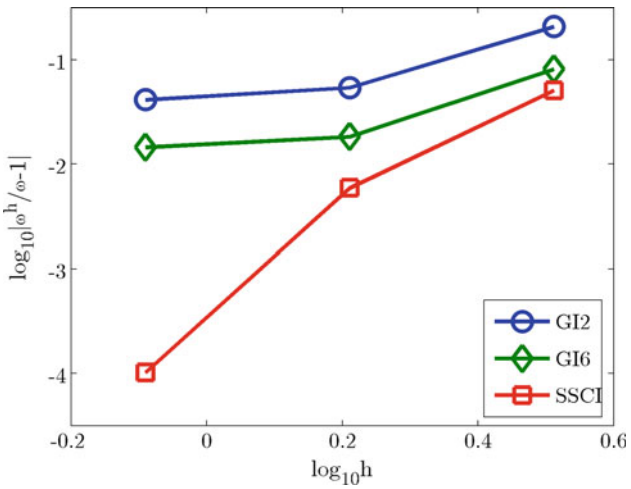

Fig. 22 Comparison of the second frequency for clamped square plate

corresponding results in Figs. 10, 11 and 12 once again confirm that the SSCI method performs superiorly compared to GI2 and GI6.

4.2 Simply supported square plate

Consider a simply supported square plate as shown in Fig. 13. The geometry and material properties are: length $a = 10$, thickness $t = 0.05$, density $\rho = 8000$, Young's modulus $E = 2 \times 10^{11}$, and Poisson ratio $\upsilon = 0.3$. Three meshfree discretizations used in the analysis are shown in Fig. 14. The quadratic basis and the cubic B-spline kernel function with a normalized support size of 1.3 are employed in the HRK approximation. Figures 15 and 16 show the comparisons of the fundamental and second frequencies obtained by using different methods. Moreover the circular frequencies for modes 1–8 as shown in Fig. 17 using the third discretization are presented in Table 1. Here for convenience of presentation a dimensionless natural frequency $\lambda = (\omega a^2\sqrt{\rho t/D})^{1/2}$ with D being flexural rigidity $D = Et^3/[12(1-\upsilon^2)]$, is introduced. Similar meaning holds for λ the following examples. It is observed that the results using SSCI agree well with the analytical solutions and compared favorably with GI2 and GI6. Meanwhile, Fig. 19 shows the results corresponding to the random non-uniform discretizations as listed in Fig. 18. It can be clearly seen that in case of irregular dicsretizations the present method still yields the most favorable solution accuracy compared to GI2 and GI6.

Table 2 List of λs for clamped square plate

Mode	Analytical [46]	GI2	GI6	SSCI
1	5.999	6.016	6.007	5.997
2	8.567	8.618	8.587	8.567
3	8.567	8.618	8.587	8.567
4	10.402	10.454	10.435	10.390
5	11.486	11.598	11.515	11.478
6	11.486	11.625	11.541	11.506
7	12.845	12.943	12.903	12.827
8	12.845	12.943	12.903	12.829

Fig. 23 Mode shapes for clamped square plate

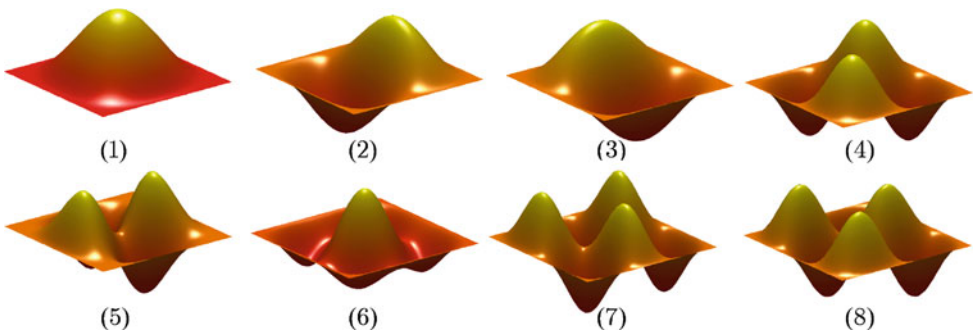

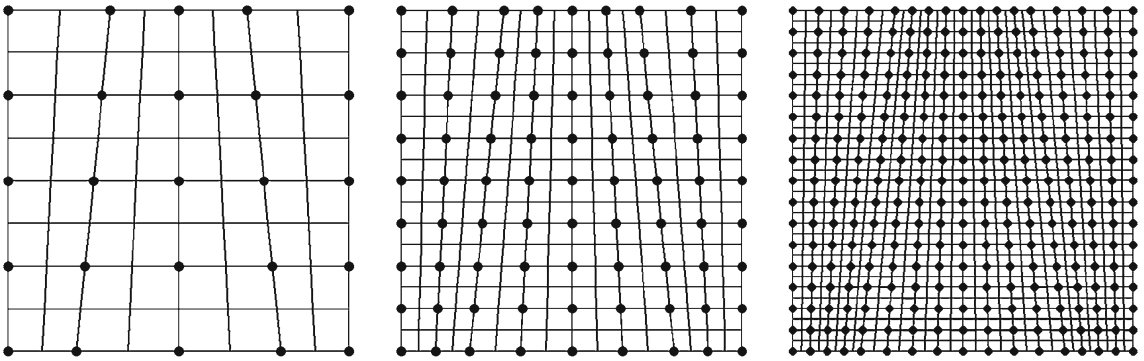

Fig. 24 Irregular discretizations for clamped square plate

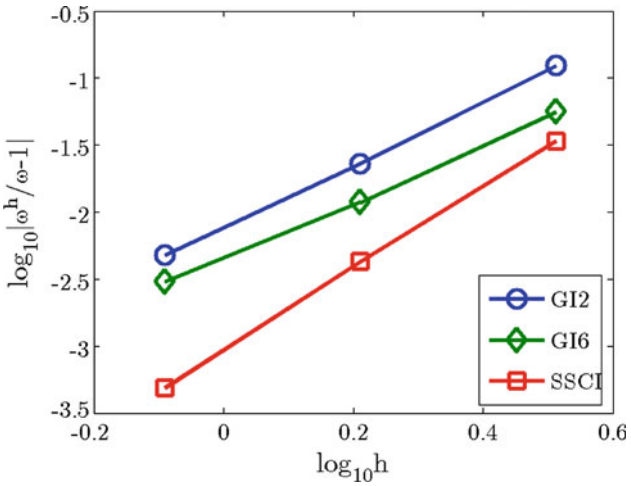

Fig. 25 Comparison of the second frequency for clamped square plate using irregular discretizations

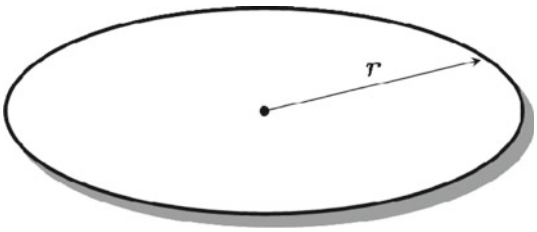

Fig. 26 A clamped circular thin plate

4.3 Clamped square plate

A clamped square plate is shown in Fig. 20. The geometry and material parameters are the same as those of the previous simply supported square plate, and the meshfree discretizations are also listed in Fig 14. Also the quadratic basis with normalized support size of 1.3 for the B-spline kernel function is employed. The results of the fundamental and second frequencies using different methods are shown in Figs. 21 and 22. The vibration shapes of modes 1–8 are listed in Fig. 23 and for more details the dimensionless natural circular frequencies using various integration schemes are tabulated in Table 2 as well. The results again uniformly confirmed that the SSCI solutions have good agreement with the analytical solutions and they compares superiorly with those obtained by GI2 and GI6. The non-uniform dicretizations as shown in Fig. 24 is also used to further verify the proposed methodology. The numerical results are plotted in Fig. 25 and they evince that compared to GI2 and GI6, the present method gives the lowest solution errors and is robust for the irregular discretizations.

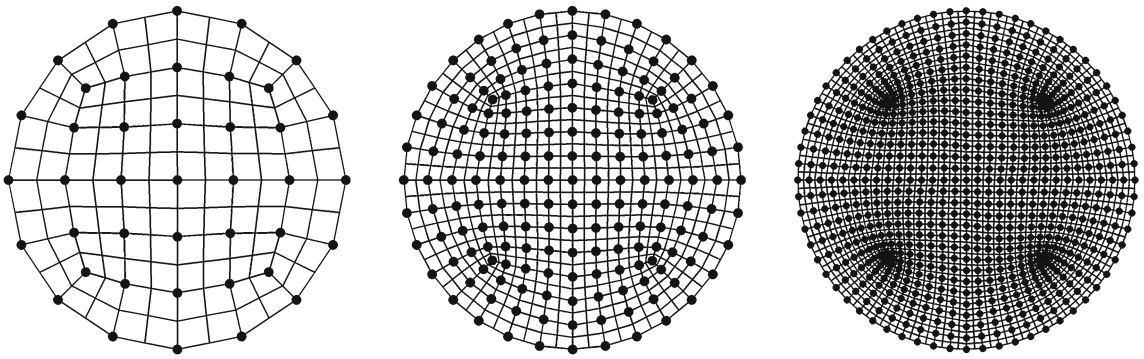

Fig. 27 Meshfree discretizations for circular plate

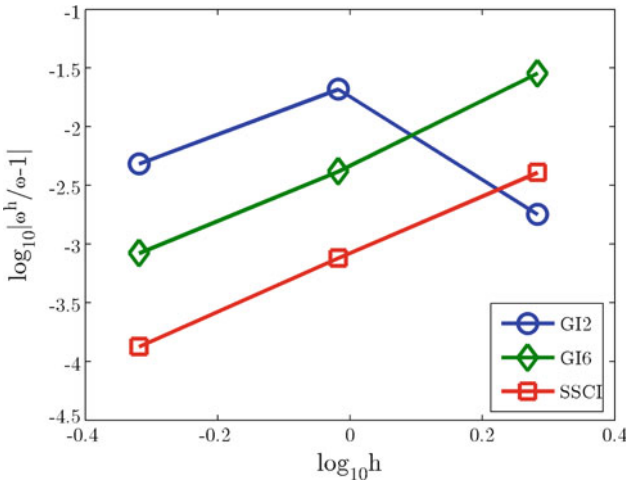

Fig. 28 Comparison of the fundamental frequency for clamped circular plate

4.4 Clamped circular plate

As shown in Fig. 26, a clamped circular plate is considered. The material and geometry parameters are density $\rho = 8000$, Young's modulus $E = 2 \times 10^{11}$, Poisson ratio $\upsilon = 0.3$, plate radius $r = 5$, and thickness $t = 0.05$. Figure 27 shows the progressive refinement of meshfree discretizations. The HRK approximation with quadratic bases and cubic B-spline kernel function with normalized support size of 1.3 are used. The convergence behavior of the fundamental frequency is shown in Fig. 28 and the results of the first eight dimensionless natural circular frequencies corresponding to the modes 1–8 listed in Fig. 29 using the third meshfree discretization are summarized in Table 3. The results also show that the present SSCI approach performs superiorly compared to GI2 and GI6. Moreover the wiggle convergence behavior of GI2 as shown in Fig. 28 indicates that the GI2 solutions are not stable in this case.

4.5 Clamped rhombic plate

The clamped rhombic thin plate as shown in Fig. 30 is a benchmark problem to test the robustness of numerical methods. The material and geometry properties for this rhombic plate are: density $\rho = 8000$, Young's modulus $E = 2 \times 10^{11}$, Poisson ratio $\upsilon = 0.3$, plate length $a = 10$, width $b = 20$, and thickness $t = 0.05$. The meshfree discretizations are shown in Fig. 31. The normalized support size of 1.5 is employed in the cubic B-spline kernel function with quadratic HRK approximation. The comparison of the fundamental frequency using various integration methods is shown

Table 3 List of λs for clamped circular plate

Mode	Analytical [28]	GI2	GI6	SSCI
1	3.196	3.188	3.197	3.196
2	4.611	4.600	4.614	4.609
3	4.611	4.600	4.614	4.609
4	5.906	5.877	5.912	5.901
5	5.906	5.908	5.913	5.901
6	6.306	6.304	6.311	6.303
7	7.144	7.127	7.157	7.134
8	7.144	7.127	7.157	7.135

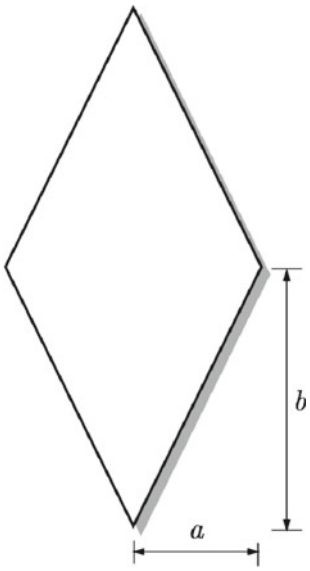

Fig. 30 A clamped rhombic thin plate

Fig. 29 Mode shapes for clamped circular plate

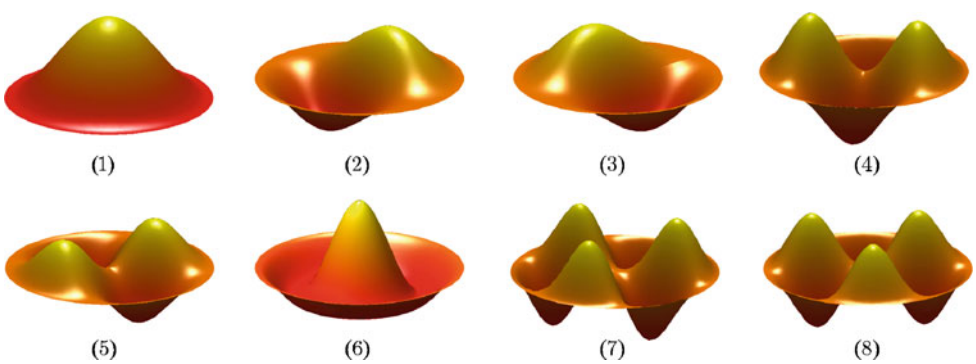

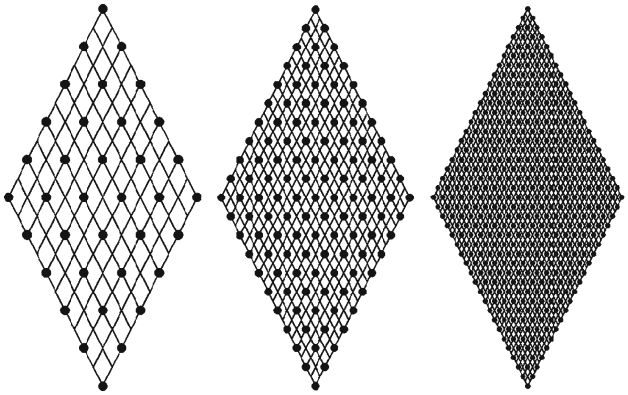

Fig. 31 Meshfree discretization for clamped rhombic plate

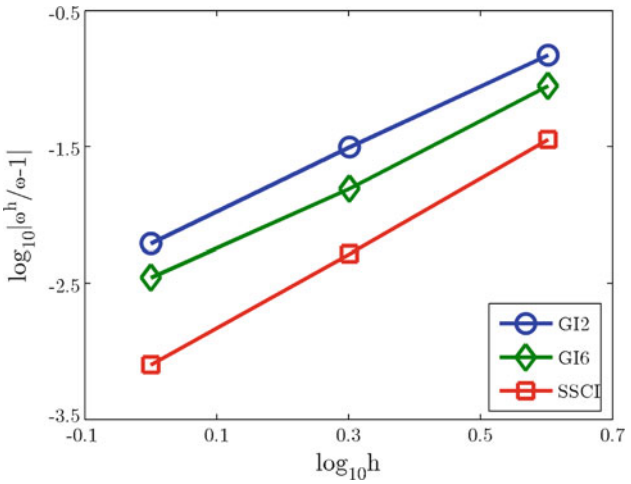

Fig. 32 Comparison of the fundamental frequency for clamped rhombic plate

in Fig. 32 and Fig. 33 shows the shapes of modes 1–8. The dimensionless natural frequencies of modes 1–7 for clamped rhombic plate are listed in Table 4. All the results demonstrate that the best solution accuracy is observed for the proposed SSCI method.

5 Effect of sub-domain refinement

In the previous typical thin plate examples it was shown that 2 by 2 sub-domains are capable of yielding accurate numerical solutions, where a quadrilateral is used as a sub-domain. In this section the influence of sub-domain refinement on the solution accuracy is further studied. The sub-division of the quadrature sub-domain Ω_{L_m} is shown in Fig. 34, in which Ω_{L_m} is further divided into two triangles, i.e., $\Omega_{L_{m1}}$ and $\Omega_{L_{m2}}$. Consequently there are eight triangular sub-domains in each nodal representative domain for the SSCI integration, as is termed as SSCI-T8 and for comparison SSCI-Q4 is used to denote the 2 by 2 sub-domain integration employed in the previous examples. The sub-domain integration refinement and numerical solutions using the refined sub-domain integration method for the simply supported square plate, the clamped square plate, the clamped circular plate, and the clamped rhombic plate, are systematically shown in Figs. 35, 36, 37, 38, 39, 40 and 41. The material and geometry properties are the same as the examples in the previous section. The numerical results reveal that the SSCI-T8 solutions exhibit the lowest errors and the sub-domain refinement has the capability of further improving the solution accuracy. It is noted that even for SSCI-T8 there still only has eight sampling points which is much smaller than the number of integration points of GI6, i.e., 36 sampling points. Moreover the

Table 4 List of λs for clamped rhombic plate

Mode	Analytical [47]	GI2	GI6	SSCI
1	8.004	8.054	8.032	7.998
2	13.640	13.781	13.712	13.627
3	18.679	18.922	18.814	18.685
4	19.534	19.780	19.692	19.501
5	26.539	26.927	26.821	26.467
6	28.415	28.993	28.701	28.431
7	32.818	33.395	33.186	32.799

Fig. 33 Mode shapes for clamped rhombic plate

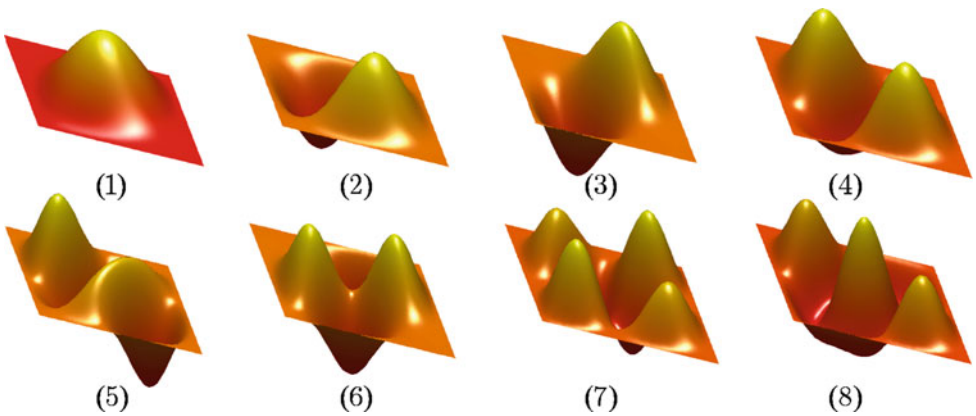

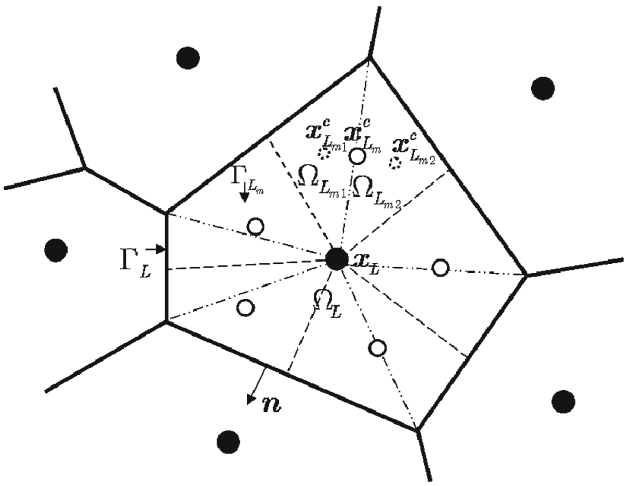

Fig. 34 Schematic illustration of refinement of sub-domain integration

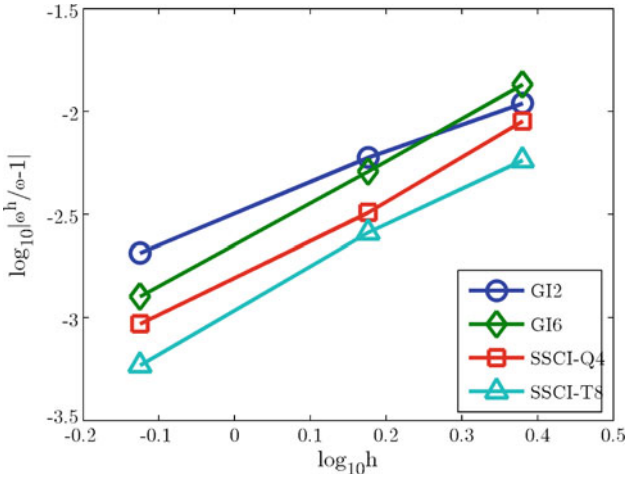

Fig. 36 Comparison of the fundamental frequency for simply supported square plate with sub-domain refinement

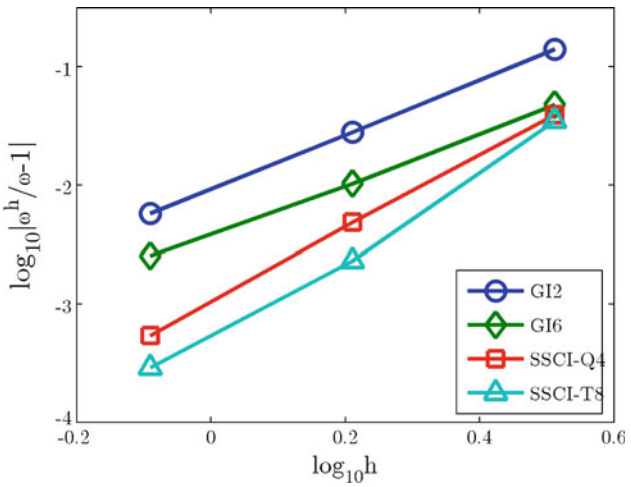

Fig. 37 Comparison of the fundamental frequency for clamped square plate with sub-domain refinement

condition of integration constraint associated with bending exactness is also exactly met regardless of the number of integration sub-domains.

6 Conclusions

A Hermite reproducing kernel (HRK) Galerkin meshfree formulation was proposed for the free vibration analysis of thin plate structures. The present approach is featured by the HRK approximation and sub-domain stabilized conforming integration (SSCI). In the HRK approximation both the deflectional and rotational degrees of freedom at a generic field point are considered to construct the approximation of the primary deflection variable by simultaneously imposing the reproducing or consistency conditions on the deflection and rotations. Through a typical 2D example it was shown that the HRK approximation has a smaller necessary support size for the kernel function from the point of view of moment matrix invertibility. Moreover it was demonstrated that with the reduced support size of kernel function the resulting HRK shape functions still exactly satisfies the consistency conditions.

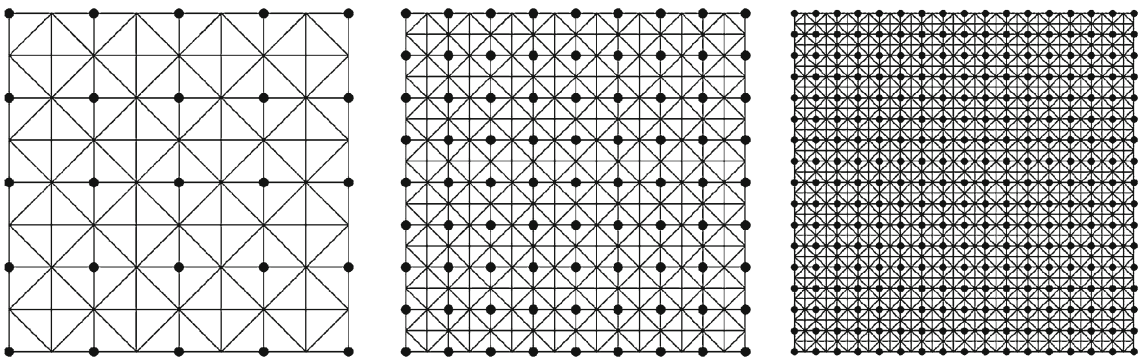

Fig. 35 Refinement of sub-domains for square plate

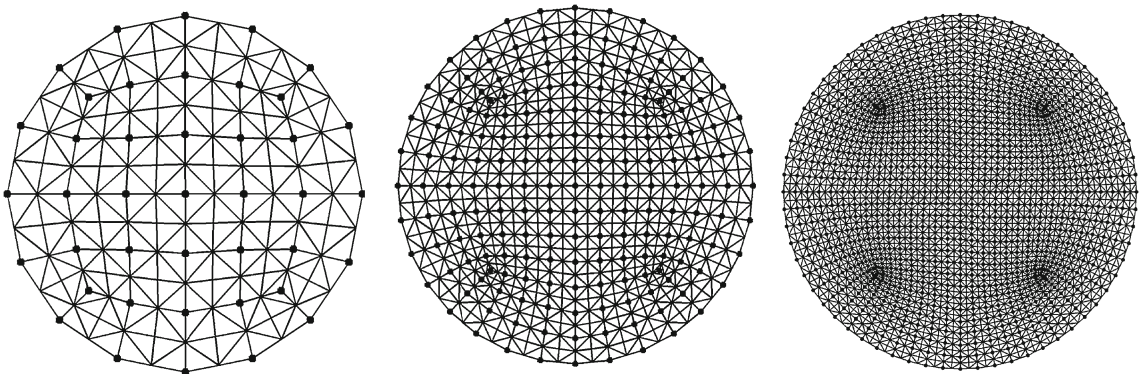

Fig. 38 Refinement of sub-domains for circular plate

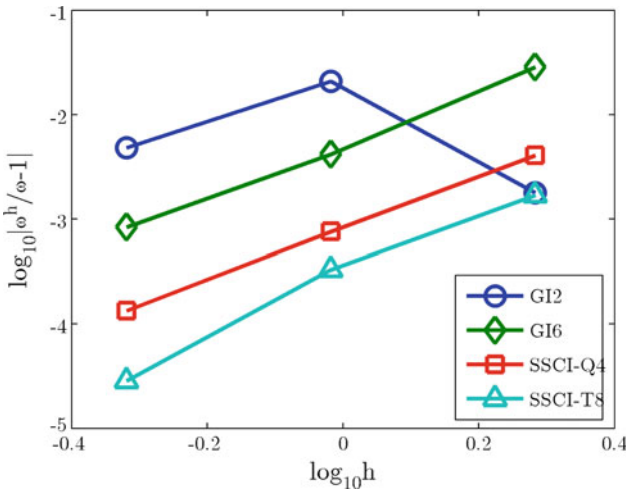

Fig. 39 Comparison of the fundamental frequency for clamped circular plate with sub-domain refinement

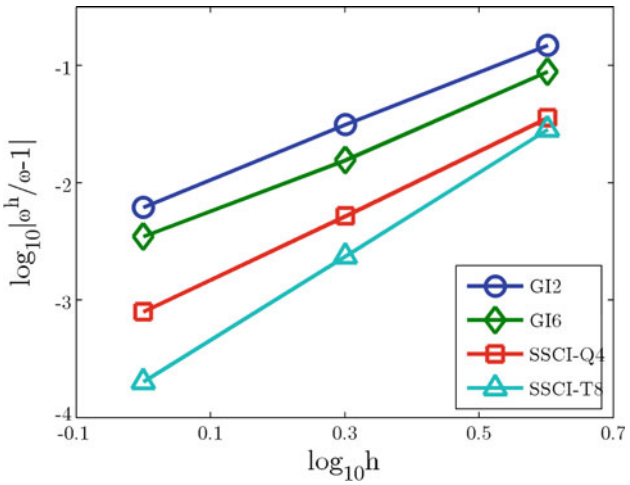

Fig. 41 Comparison of the fundamental frequency for clamped rhombic plate with sub-domain refinement

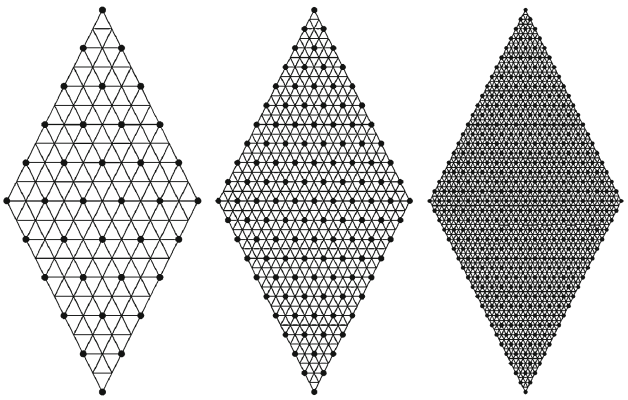

Fig. 40 Refinement of sub-domains for rhombic plate

Meanwhile the domain integration for both the mass and stiffness matrices was consistently carried out by using the method of SSCI. For the stiffness the SSCI was implemented through the sub-domain curvature smoothing, while the integration for the mass matrix was performed by sampling the centroid density values over the sub-domains and then multiplying the corresponding sub-domain areas. In the static sense this approach exactly meets the integration constraint for bending exactness regardless of the number of sub-domains used for numerical quadrature. Numerical solutions for the presented benchmark vibration examples uniformly demonstrated that the proposed method performs superiorly compared to the approach based higher order Gauss integration. Moreover the effect of sub-domain refinement on the solution accuracy was also investigated and it was found from typical numerical examples that this integration refinement yields an enhancement of solution accuracy.

Acknowledgments The financial support of this work by the National Natural Science Foundation of China (10972188, 10602049) and the Program for New Century Excellent Talents in University from China Education Ministry (NCET-09-0678) is gratefully acknowledged.

References

1. Belytschko T, Lu YY, Gu L (1994) Element-free Gakerkin methods. Int J Numer Methods Eng 37:229–256
2. Belytschko T, Kronggauz Y, Organ D, Fleming M (1996) Meshless methods: an overview and recent developments. Comput Methods Appl Mech Eng 139:3–47
3. Belytschko T, Guo Y, Liu WK, Xiao SP (2000) Unified stability analysis of meshless particle methods. Int J Numer Methods Eng 48:1359–1400
4. Liu WK, Jun S, Zhang YF (1995) Reproducing kernel particle methods. Int J Numer Methods Fluids 20:1081–1106
5. Liu WK, Jun S, Li S, Adee J, Belytschko T (1995) Reproducing kernel particle methods for structural dynamics. Int J Numer Methods Eng 38:1665–1679
6. Liu WK, Jun S (1998) Multiple-scale reproducing kernel particle methods for large deformation problems. Int J Numer Methods Eng 41:1339–1362
7. Chen JS, Pan C, Wu CT, Liu WK (1996) Reproducing kernel particle methods for large deformation analysis of nonlinear structures. Comput Methods Appl Mech Eng 139:195–227
8. Li S, Liu WK (2002) Meshfree and particle methods and their applications. Appl Mech Rev 55:1–34
9. Babuška I, Banerjee U, Osborn JE (2003) Survey of meshless and generalized finite element methods: a unified approach. Acta Numerica 12:1–125
10. Huerta A, Belytschko T, Fernández-Méndez S, Rabczuk T (2004) Meshfree methods. Encyclopedia Comput Mech 1:279–309
11. Li S, Liu WK (2004) Meshfree particle methods. Springer, Berlin
12. Liu GR (2009) Mesh free methods: moving beyond the finite element method, 2nd edn. CRC Press, Boca Raton
13. Lancaster P, Salkauskas K (1981) Surfaces generated by moving least squares methods. Math Comput 37:141–158
14. Krysl P, Belytschko T (1995) Analysis of thin plates by the element-free Galerkin method. Comput Mech 16:1–10
15. Krysl P, Belytschko T (1996) Analysis of thin shells by the element-free Galerkin method. Int J Solids Struct 33: 3057–3080
16. Liu GR, Chen XL (2001) A meshfree method for static and free vibration analyses of thin plates of complicated shape. J Sound Vib 241:839–855
17. Liu L, Liu GR, Tan VBC (2002) Element free method for static and free vibration analysis of spatial thin shell structures. Comput Methods Appl Mech Eng 191:5923–5942
18. Li S, Hao W, Liu WK (2000) Numerical simulations of large deformation of thin shell structures using meshfree method. Comput Mech 25:102–116
19. Qian D, Eason T, Li S, Liu WK (2008) Meshfree simulation of failure modes in thin cylinders subjected to combined loads of internal pressure and localized heat. Int J Numer Methods Eng 76:1159–1184
20. Zhou JX, Zhang HY, Zhang L (2005) Reproducing kernel particle method for free and forced vibration analysis. J Sound Vib 279:389–402
21. Long SY, Atluri SN (2002) A meshless local Petrov–Galerkin method for solving the bending problem of a thin plate. CMES: Comput Modeling Eng Sci 3:53–63
22. Rabczuk T, Areias PMA, Belytschko T (2007) A meshfree thin shell method for nonlinear dynamic fracture. Int J Numer Methods Eng 72:524–548
23. Liu WK, Han W, Lu H, Li S, Cao J (2004) Reproducing kernel element method. Part I. Theoretical formulation. Comput Methods Appl Mech Eng 193:933–951
24. Li S, Lu H, Han W, Liu WK, Simkins DC (2004) Reproducing kernel element method. Part II. Global conforming I^m/C^n hierarchy. Comput Methods Appl Mech Eng 193:953–987
25. Lu H, Li S, Simkins DC, Liu WK, Cao J (2004) Reproducing kernel element method. Part III. Generalized enrichment and applications. Comput Methods Appl Mech Eng 193:989–1011
26. Simkins DC, Li S, Lu H, Liu WK (2004) Reproducing kernel element method. Part IV. Globally compatible $C^n (n \geq 1)$ triangular hierarchy. Comput Methods Appl Mech Eng 193:1013–1034
27. Simkins DC (2004) General reproducing kernel element hierarchies. PhD thesis, University of California, Berkeley
28. Chen JT, Chen IL, Chen KH, Lee YT, Yeh YT (2004) A meshless method for free vibration analysis of circular and rectangular clamped plates using radial basis function. Eng Anal Boundary Elem 28:535–545
29. Liu Y, Hon YC, Liew KM (2005) A meshfree Hermite-type radial point interpolation method for Kirchhoff plate problems. Int J Numer Methods Eng 66:1153–1178
30. Cui X, Liu GR, Li G (2009) A smoothed Hermite radial point interpolation method for thin plate analysis. Arch Appl Mech. doi:10.1007/s00419-009-0392-0
31. Chen JS, Wu CT, Belytschko T (2000) Regularization of material instabilities by meshfree approximations with intrinsic length scales. Int J Numer Methods Eng 47:1301–1322
32. Beissl S, Belytschko T (1996) Nodal integration of the element-free Galerkin method. Comput Methods Appl Mech Eng 139:49–64
33. Belytschko T, Xiao SP (2002) Stability analysis of particle methods with corrected derivatives. Comput Math Appl 43:329–350
34. Chen JS, Wu CT, Yoon S, You Y (2001) A stabilized conforming nodal integration for Galerkin meshfree methods. Int J Numer Methods Eng 50:435–466
35. Chen JS, Yoon S, Wu CT (2002) Nonlinear version of stabilized conforming nodal integration for Galerkin meshfree methods. Int J Numer Methods Eng 53:2587–2615
36. Wang D, Chen JS (2004) Locking-free stabilized conforming nodal integration for meshfree Mindlin–Reissner plate formulation. Comput Methods Appl Mech Eng 193:1065–1083
37. Chen JS, Wang D, Dong SB (2004) An extended meshfree method for boundary value problems. Comput Methods Appl Mech Eng 193:1085–1103
38. Wang D, Chen JS (2004) Constrained reproducing kernel formulation for shear deformable shells. In: Proceeding of the 6th world congress on computational mechanics, Beijing, China, September 5–10
39. Wang D, Dong SB, Chen JS (2006) Extended meshfree analysis of transverse and inplane loading of a laminated anisotropic plate of general planform geometry. Int J Solids Struct 43:144–171
40. Wang D, Chen JS (2006) A locking-free meshfree curved beam formulation with the stabilized conforming nodal integration. Comput Mech 36:83–90
41. Chen JS, Wang D (2006) A constrained reproducing kernel particle formulation for shear deformable shell in Cartesian coordinates. Int J Numer Methods Eng 68:151–172
42. Wang D, Wu Y (2008) An efficient Galerkin meshfree analysis of shear deformable cylindrical panels. Interaction Multiscale Mech 1:339–355
43. Wang D (2006) A stabilized conforming integration procedure for Galerkin meshfree analysis of thin beam and plate. In: Proceedings of the 10th enhancement and promotion of computational methods in engineering and science, Sanya, China, August 21–23
44. Wang D, Chen JS (2008) A Hermite reproducing kernel approximation for thin plate analysis with sub-domain stabilized conforming integration. Int J Numer Methods Eng 74:368–390

45. Chen JS, Wang HP (2000) New boundary condition treatments for meshless computation of contact problems. Comput Methods Appl Mech Eng 187:441–468
46. Gorman DJ (1982) Free vibration analysis of rectangular plates. Elsevier, New York
47. Gorman DJ (1988) Accurate free vibration analysis of rhombic plates with simply-supported and fully-clamped edge conditions. J Sound Vib 125:281–290